Geophysical Journal International

Geophys. J. Int. (2013) **192,** 413–424 doi: 10.1093/gji/ggs034

Noise directivity and group velocity tomography in a region with small velocity contrasts: the northern Baltic shield

P. Poli, H. A. Pedersen, M. Campillo; and the POLENET/LAPNET Working Group

ISTerre, Université de Grenoble I, CNRS, BP 53, *F*-38041 *Grenoble Cedex* 9, *France. E-mail: polip@ujf-grenoble.fr*

Accepted 2012 October 16. Received 2012 October 15; in original form 2012 May 14

SUMMARY

Ambient noise tomography (ANT) is widely used to image strong velocity variations within the upper crust. Using careful processing, we obtained a 3-D model of shear velocities in the upper crust beneath northern Finland, where the lateral velocity variations are less than 3 per cent. As part of the tomography, the noise field is analysed. It is strongly heterogeneous but the signal-to-noise ratio is sufficient to obtain stable dispersion curves for all profile azimuths. Our results show that the directions of dominant noise sources of Rayleigh and Love waves are the same, but the amplitude distribution with azimuth is different for the two types of waves. More intriguingly, the high frequency Love waves are dominated by a mixture of higher modes rather than the fundamental mode. The reconstructed 3-D model shows the Lapland Granulite Belt as a high velocity body with a limit at surface in excellent agreement with geological observations at surface. Following this interface at depth, our results are compatible with previous studies suggesting an Archean north oriented subduction.

Key words: Interferometry; Seismic tomography; Cratons; Crustal structure.

1 INTRODUCTION

Ambient noise tomography (ANT) is a recently developed branch of seismology for which one major application is crust and upper mantle surface wave tomography. Instead of relying in the presence of transient sources, ANT is based on correlation of a random wavefield to extract the Green's function (Campillo & Paul 2003; Shapiro & Campillo 2004; Sabra *et al.* 2005a; Pedersen *et al.* 2007; Gouédard *et al.* 2008). With this technique, it is possible to overcome a series of classical problems in surface wave tomography, in particular the lack of homogeneous distributed transient sources, and the difficulty of extracting the high frequency part of dispersion curves in the case of distant sources. ANT is however not free of difficulties, related to the distribution of the noise sources. First, the sources are mainly located at the surface. This may actually be an advantage to ANT as the extracted records are dominated by surface waves. Second, as the noise sources are unevenly distributed at the surface (Stehly *et al.* 2006) the observed surface wave velocities may be biased (Pedersen *et al.* 2007; Yao & van der Hilst 2009; Froment *et al.* 2010).

Spectacular applications can be fund all over the world (e.g. Shapiro *et al.* 2005; Sabra *et al.* 2005b; Stehly *et al.* 2009; Ritzwoller *et al.* 2011). Most studies have focused on areas with strong velocity variations (typically up to ±5–20 per cent), as those observed between sediments and bedrock. In such cases the possible bias and/or lack of precision in dispersion measurements using estimated Green's functions is smaller than the retrieved velocity variations in the model, and high-resolution tomography is robust, as shown by the similar results obtained by the two independent studies of Sabra *et al.* (2005b) and Shapiro *et al.* (2005).

In the absence of sediments or if the crustal rock composition does not vary significantly across the study area, seismic velocities typically vary less than ±3 per cent. Examples of such challenging areas are cratons, which are presently subject to much attention as a key to understanding the evolution of the early Earth, and due to their strategic role for ore exploration. In this case, the lateral velocity variations may be smaller than the errors associated with ANT, so particular care must be taken during all processing steps to achieve a good signal-to-noise ratio (SNR) for a wide range of azimuths. Recently, Prieto *et al.* (2011) and Poli *et al.* (2012) demonstrated that using small time windows is a more efficient way to ensure a good Green's function estimation than using 1-d time windows. These studies show that there are still significant improvements in ANT through refining the processing methods.

In this article we use ANT to obtain a 3-D *Vs* model of northern Fennoscandia. This zone is a stable cratonic area where velocity variations from previous models are in the range of ±3 per cent or less (Janik *et al.* 2009). The complex geometry of tectonic units at the surface, leading to a variety of models for the tectonic evolution of the area, does not translate into lateral major velocity variations in the crust. The only 'major' velocity contrast observed on 2-D active seismic profiles is created by a high velocity upper crustal body (+3 per cent) which is interpreted as a remnant slice of Archean crust, related with an Archean subduction event (Janik *et al.* 2009, and reference therein).

We first present the processing that we apply, after which we analyse the directivity of the noise field and the modal composition of the extracted surface waves. Special attention was given to the extraction of Love waves, as they give complementary information to the Rayleigh waves through different sensitivity, and insight to radial anisotropy. In this study, we bring some additional understanding of the origin of these difficulties as the absence of sedimentary basins facilitates the interpretation of the observed Love wave. We subsequently measure group velocities for all station profiles and calculate group velocity maps for a series of frequencies. These group velocity maps are used as input to an inversion aimed at the 3-D model of shear velocities.

2 DATA PROCESSING AND NOISE WAVEFIELD

We analyse seismic data continuously recorded during the POLENET/LAPNET temporary experiment (Kozlovskaya *et al.* 2006) in northern Fennoscandia. The array configuration (Fig. 1) is approximately a 2-D grid with station separations that span from ∼50 to ∼600 km. We used records for the calendar year 2008 during which the array was fully operational. Standard preprocessing was applied, including removing mean and data trend, pre-filtering (0.01–2 Hz), resampling to identical sample rate (5 Hz) and deconvolution of the instrumental responses. In this section, we present in some detail the processing used to estimate the Green's function after which we present the characteristics of the noise field.

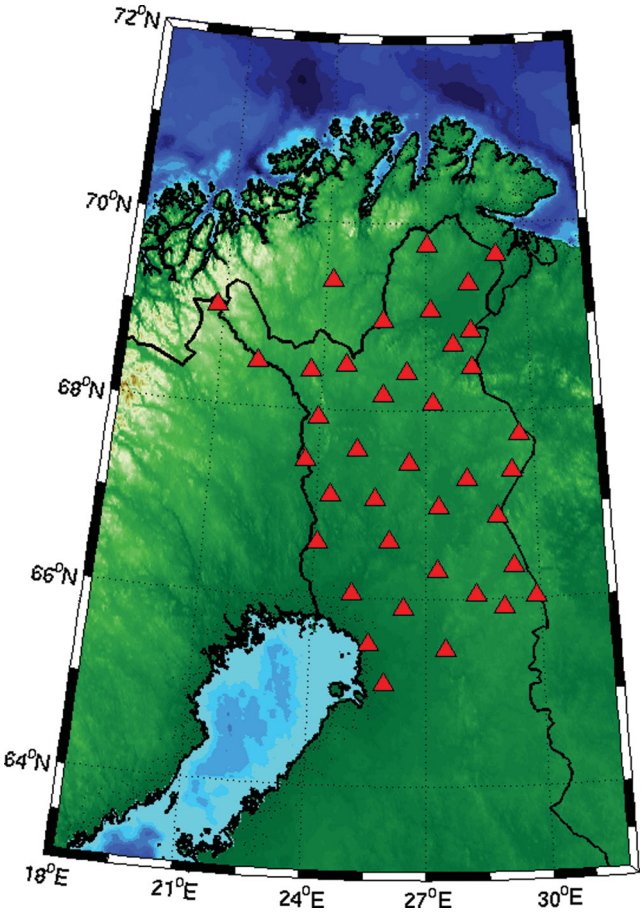

Figure 1. Map of the study area: red triangles are the seismic broad-band stations.

2.1 Green's function estimation

To be able to extract Rayleigh and Love waves we calculated ZZ and TT noise cross-correlations using vertical–vertical and transverse–transverse (TT) components. Many groups are presently addressing the issue of how to calculate the 'best' quality Green's function estimates, in terms of symmetry, SNR, and frequency bandwidth. No universal processing method has yet emerged, and it may well be that the processing needs to be adapted to the target type of wave and frequency content as well as the study area. We therefore carried out a series of tests to using different approaches, and quantify the quality of the estimated Green's functions.

Poli *et al.* (2012) used a processing procedure, which effectively made it possible to extract the body wave part of the Green's function. Different from standard noise correlation processing, they used short time windows (4 hr). No time domain (e.g. one-bit) normalization was applied, but all time windows were statistically analysed and removed if amplitudes larger than 10 times the standard deviation of the data were fund. Then the spectrum of the noise data is normalized using a whitening function. This approach was used to reduce the effect of transient sources and instrumental problems while obtaining a broad-band correlation.

To verify whether this processing is adequate for surface wave tomography in our study area, we compared the resulting noise correlations with noise correlations obtained using (i) 1-bit normalization (Campillo & Paul 2003; Shapiro & Campillo 2004), and (ii) running-absolute-mean normalization (Bensen *et al.* 2007). For the latter, we used a width of the moving window of 10 s, which is equal to half of the maximum period used in the tomography. We here show representative results using vertical component data from two stations located approximately 200 km apart.

Following procedures by, for example, Groos *et al.* (2012), we use two parameters to estimate the quality of the obtained Rayleigh wave GF. The correlation coefficient ('*R*') provides the convergence rate in time (months) towards a reference correlation function ref:

$$R(j) = \frac{\Theta(j, \mathrm{ref})}{\sqrt{\Theta(\mathrm{ref}, \mathrm{ref})\Theta(j, j)}},$$

where $\Theta(j, \mathrm{ref})$ is the correlation between correlation j and the reference correlation ref, and $C(j, j)$ and $C(ref, ref)$ are their autocorrelations. Here *ref* is the reference correlation (averaged over 12 months) and *j* the correlation function averaged over months 1 to *j*.

The 'SNR' of the folded correlations illustrates how the Green's functions emerge from the remnant oscillations of the noise:

$$SNR(j) = \frac{\max[signal(j)]}{rms[noise(j)]},$$

where *signal*(*j*) is the correlation function within the time window delimited by group velocities 3 and 4 km s^{-1} and *noise*(*j*) is the 1000 s tail of the correlation function. In both *signal*(*j*) and *noise*(*j*) the correlation function is stacked over months 1 to *j*.

Fig. 2 shows *R*(*j*) and *SNR*(*j*) for the different types of processing. First, we evaluate the benefit obtained by using 4 hours time windows as compared to 24 hours time windows. For both R (Fig. 2a) and SNR (Fig. 2b) we observe that correlations calculated with shorter time windows (black lines) converge significantly more rapidly than for longer time windows (black dashed lines) and that the SNR is improved approximately by a factor of two.

The comparison of R and SNR for the processing of Poli *et al.* (2012) using 4 hr windows (black lines) with one-bit correlation (red lines) and running-absolute-mean correlation (blue

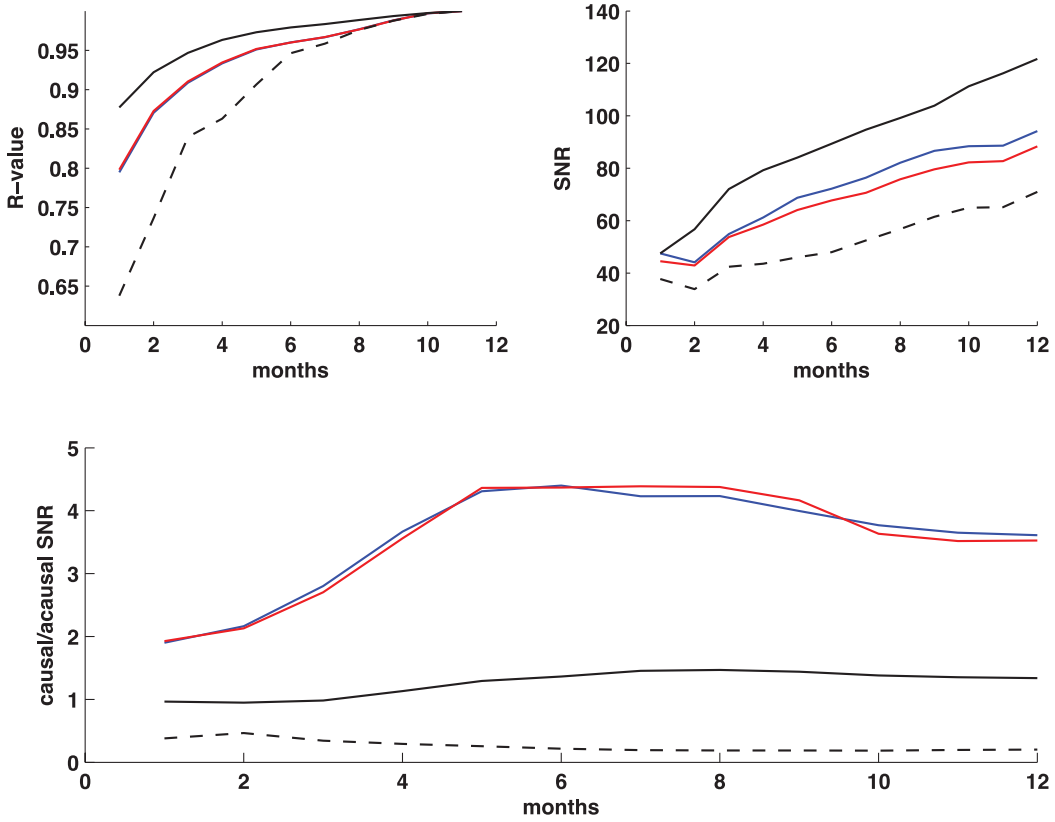

Figure 2. Comparison of the different processing: (a) *R*-value as function of time averaging for the processing using one-bit correlation with four hour windows (blue line), moving average with four hour windows (red line) and the processing suggested by Poli *et al.* (2012) with four hour windows (black solid line) and 24-hr windows (black dashed line). (b) SNR as a function of time averaging. The colour code is the same as in (a). (c) Symmetry of the correlation function evaluated as the ratio of SNR at causal and acausal parts of the estimated Green's function. Perfect symmetry would imply unit ratio.

lines), calculated using 4 hr windows shows that the former provides a faster rate of convergence, with a SNR that is 1.3 larger than the one observed for one-bit or running-absolute-mean correlations.

We also estimate the symmetry of the GF for the different processing approaches. Fig. 2(c) shows the ratio between the causal and acausal SNR. Note that perfectly symmetric GF would have a ratio equal to one. Also this criterion shows that our processing is efficient for the study area. Fig. 2 does also shows some limitations of using this criterion to estimate the quality of the GF, as the ratio rapidly reaches a constant value over time while the SNR still increases.

Following these results, we proceeded to the calculation of the noise correlation as in Poli *et al.* (2012).

2.2 Directivity of seismic noise

Since the SNR of the correlations is an estimate of the coherent surface wave energy contained in the noise wave-field, we use SNR of non-folded correlations to provide insight to the azimuth distribution of the incoming noise in different frequency bands. In Figs 3(a) and (b), the SNR for 1 yr averaged Love (blue lines) and Rayleigh (red lines) waves is shown as a function of azimuth, and for the period ranges 10–20 s (Fig. 3a) and 2–10 s (Fig. 3b). The SNR value is evaluated every 10° of azimuth, by averaging the SNR over a sliding 10° wide non-overlapping azimuth window. Individual traces may therefore have a smaller SNR than that reported onto this figure. To better understand the noise sources in the area, we additionally calculated the directivity of the noise over the year, for both Rayleigh (Figs 3c and e) and Love waves (Figs 3d and f). At long periods (10–20 s, Fig. 3c).

At long period (Fig. 3a), the yearly averaged Rayleigh waves have high SNR for most azimuths, while the Love wave SNR tend to decrease towards north–northwest. In this direction the Rayleigh waves SNR tend to be very high, as index of strong noise coming from Atlantic zone. The lowest SNR is in S direction for both Love and Rayleigh waves.

Rayleigh waves are preferentially excited during the winter months from sources located west of the array (SW–NW), while the energy during the summer months is somewhat dominated by energy from the east (NE–E). On the contrary, Love waves (Fig. 3d) have a more variable pattern, but are generally dominated by eastern directions throughout the year.

At short periods (2–10 s, Fig. 3b), the Rayleigh waves have a similar pattern to the one observed for long periods, with a clear minimum of yearly SNR towards the S–SE. The Love waves also have a yearly local minimum in this azimuth interval, but SNR is significantly higher towards the west than towards the east. The evolution of the noise throughout the year (Figs 3d and f) show that, in contrast with the behaviour at long periods, the short period noise is distributed over a wide azimuth range for both Rayleigh and Love waves. A dominance of noise sources towards the west is however clear for both types of waves and we still observe a minimum of sources across all southern directions.

Our longer period data corresponds to the primary microseismic peak, which is generated by the normal stress on the sea bottom

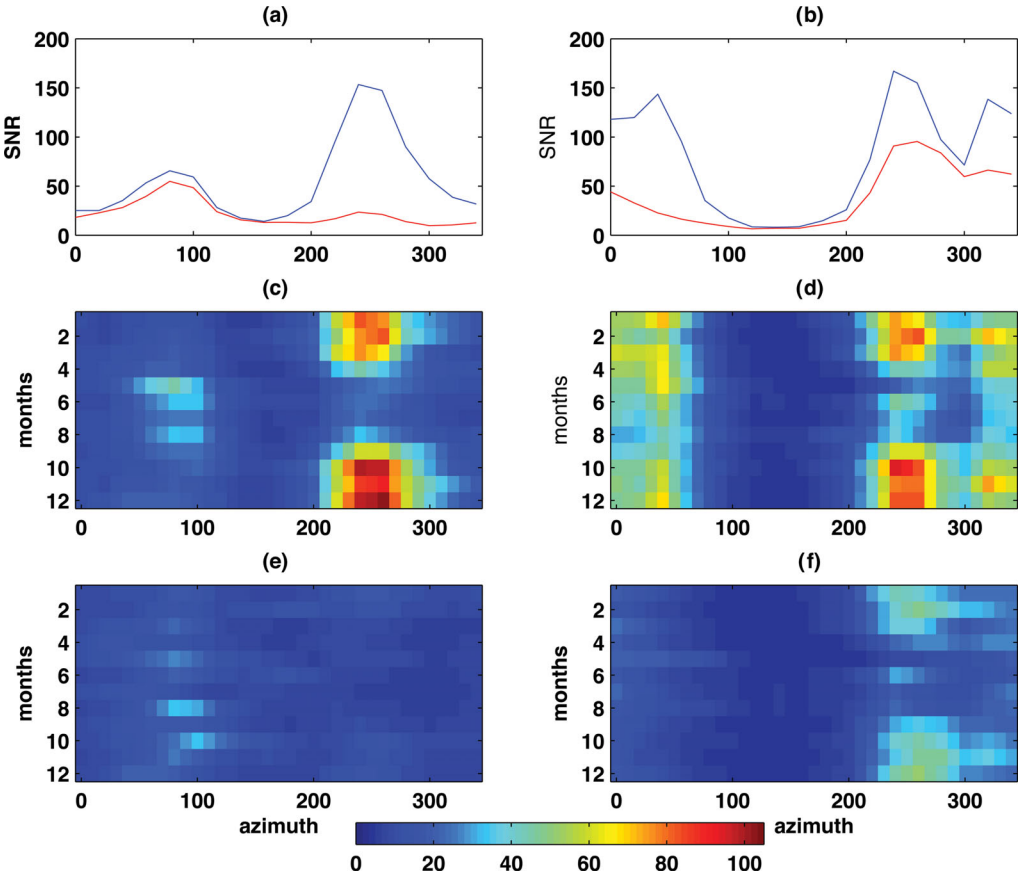

Figure 3. SNR as function of azimuth for the period range (a) 20–10 s and (b) 2–10 s for Rayleigh waves (blue dashed lines) and Love waves (red dashed lines) using 1 yr of data. (c)–(f) SNR as function of time (months) and azimuth for Rayleigh waves for period range 10–20 s (c), 1–10 s (d), Love waves for 10–20 s (e) and 1–10 s (f).

created by ocean swells (Webb *et al.* 1991; Friederich *et al.* 1998). The associated azimuthal variation of the Rayleigh wave seismic noise (Fig. 3c), shows how these sources change over time. For the winter months, our observations are compatible with previous studies, which locate the noise sources in the north Atlantic Sea, possibly dominantly SE of southern Greenland (Friederich *et al.* 1998; Stehly *et al.* 2006; Pedersen *et al.* 2007; Köhler *et al.* 2011). For the summer months, Stehly *et al.* (2006) show a predominance of noise sources in the southern hemisphere while we rather observe small amplitude noise sources located towards N–NE. We speculate that the emergence of these noise sources is related to retreating ice coverage (Stutzmann *et al.* 2009; Grob *et al.* 2011) of the Barents Sea during summer. This is compatible with low-amplitude sources towards the N–NE observed by Stehly *et al.* (2006) on seismic stations in Europe.

Our short period noise corresponds to the secondary microseismic peak, which is composed of energy generated from non-linear interaction the ocean swell, which creates a vertical force on the seafloor. The noise sources that we observe for Rayleigh waves in this frequency band (Fig. 3d) cover a wide azimuthal range across northern directions, from directions of southwest to east, and dominant western directions in the winter months. These results are in good agreements with observations and predictions by Hillers *et al.* (2012) and Ardhuin *et al.* (2011), and observations by Friederich *et al.* (1998), Pedersen *et al.* (2007) and Köhler *et al.* (2011).

Vertical forces, such as the normal forces on a flat horizontal sea bottom, solely generate energy on the P-SV component, mainly in the form of Rayleigh waves. Our observed Love waves, which have a different azimuth dependence than Rayleigh waves (see above) therefore indicate that additional mechanisms must contribute to the noise field on the SH component: either horizontal forces created by the action of swell on seafloor topography (Fukao *et al.* 2010; Saito 2010) or scattering of Rayleigh waves at lateral heterogeneities. A partial explanation for the different observations at low and high frequency may reside in the relative importance of the two mechanisms, as the scattering can be expected to increase with frequency. If Love waves are dominantly created directed by the interaction of the sea swell, we can expect to observe Love waves only in directions where we also observe Rayleigh waves. This is what we actually observe, and we therefore tentatively favor this mechanism of Love wave generation to be dominant in the frequency range we consider.

2.3 Modal analysis of seismic noise

In Fig. 4 we show the spectrogram of the correlations with the aim at understanding which modes dominate the noise field. We used the two profiles, oriented N–S and E–W, using the most distant stations available for these azimuths. For each profile we observe that the ZZ component (Figs 4a and c) is dominated by fundamental mode Rayleigh waves. The TT component (Figs 4b and d) shows a more complex behaviour. At periods larger than 10 s, the TT component is dominated by fundamental mode Love waves, while we observe a mix of higher modes at shorter periods. The sum of these higher modes could be interpreted as Lg waves (e.g. Campillo 1990).

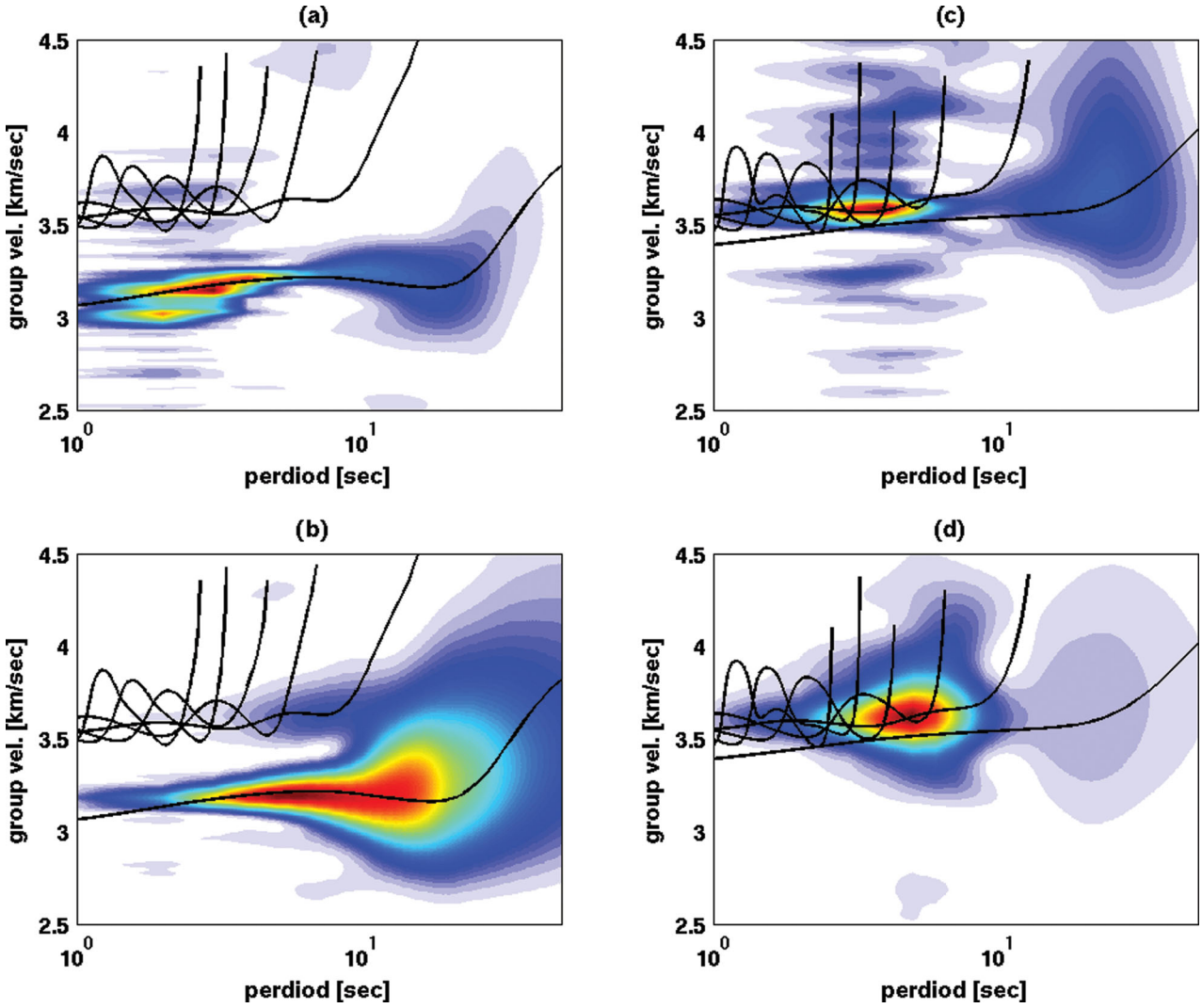

Figure 4. Example of dispersion measurement for a station pair separated by 500 km (top panel) oriented N–S, for Rayleigh (a) and Love (b) waves. Dispersion measurement for a station pair separated by 300 km (top panel) oriented E–W, for Rayleigh (a) and Love (b) waves. Theoretical dispersion curves (from model in Fig. 9a) for the firsts five modes are plotted as black lines.

Due to frequency–time analysis smoothing, the mix of higher modes of the Love waves is not easily identified in more complex tectonic settings, so erroneous interpretation of apparently continuous dispersion curves could easily occur. Our results show that the use of Love waves at periods shorter than 10 s may not be feasible in many of our measured frequency time analysis. One implication of a misidentification of the mode associated with the high frequency part of the TT dispersion curve could be a Rayleigh-Love discrepancy, which would be interpreted as radial anisotropy of the upper crust. In our case, this apparent discrepancy would lead to approximately 4 per cent anisotropy $[(V_{SH} - V_{SV})/V_{SV})$ in the top 10 km of the crust. Using Love wave phase velocities could potentially solve this problem.

Due to the difficulties of mode separation below 10 s period, and low SNR at longer periods (see selection criteria in Section 3.1), the final number of dispersion curves for Love waves was too small to reliably integrate them into the group velocity tomography. Considering the high number of reliable Rayleigh wave group velocities, we focus the subsequent tomography on Rayleigh waves.

3 FROM NOISE CORRELATION TO GROUP VELOCITY MAPS

We here focus the tomography on the analysis of the fundamental mode Rayleigh waves as observed on the ZZ component. We first measure dispersion curves for all station pairs after which we invert these dispersion curves to obtain group velocity maps for the study region.

3.1 Dispersion measurements

Group velocity dispersion curves are measured for periods of 1–50 s using frequency time analysis (Levshin *et al.* 1989). The fundamental mode Rayleigh wave was isolated using a cosine time domain window centred on predicted group velocities from an average crustal model of the area (Poli *et al.* 2012). We apply this procedure on the folded estimated GF (causal and acausal part are added, e.g. Shapiro *et al.* 2005; Verbeke *et al.* 2012). This standard procedure is well adapted to our study area as SNR for Rayleigh

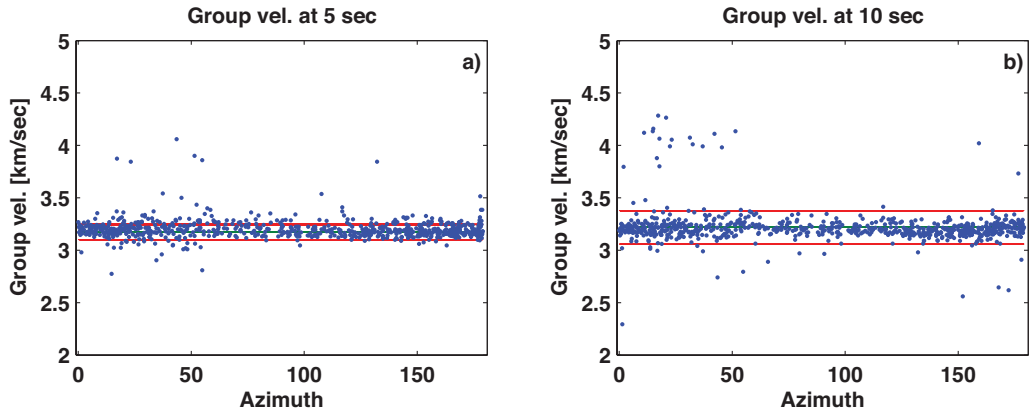

Figure 5. Azimuthal distribution of measured group velocity for Rayleigh waves at 5 s (a) and 10 s (b) period. Blue points: individual observations, Red lines: average velocity ± the standard deviation.

waves is good for both the causal and acausal part for almost all station pairs, and takes advantage of different frequency content in some cases for opposite propagation directions.

We use three criteria for rejecting observed group velocities from the tomography. First, out 861 ZZ correlation functions calculated, we retained the 745 with SNR ratio higher than 10 for either positive or negative times (or both). This ensures that at least one side of the GF is well estimated.

Second, for each profile we excluded periods beyond which the profile length was smaller than three wavelengths. At periods longer than 25 s, this criterion reduced the number of profiles to only the very longest ones, with a dominance of N–S oriented profiles, as the array dimension is bigger in this direction. We therefore decided to exclude periods longer than 25 s from the tomography to avoid N–S smearing.

Finally, velocity measurements that did not fall within two standard deviations of the mean (see also Fig. 5) were discarded, to avoid influence from these outliers. These outliers have unrealistic values as compared to the known geology of the area, and as lateral variations in upper crustal structure are known to be very small (Janik *et al.* 2009). Fig. 5 further illustrates that the group velocities have no systematic variations with azimuth. Pedersen *et al.* (2007) observed strong azimuth dependence in particular for the first microseismic peak. We attribute our improved results to first a longer observation period which enriches the azimuthal distribution of the noise sources, and second to improvements in the processing. As an illustration of this last point, Fig. 6 shows that the average group velocity curve is almost the same if we analyse correlations from three 4-month stacks rather than the stack over all 12 months.

For each dispersion curve and period, we use the variance observed for 4-months stacks as the error associated with the observed group velocity.

3.2 Calculation of group velocity maps

We inverted our dispersion measurements following the tomographic approach proposed by Barmin *et al.* (2001), and we refer to this reference paper for a detailed description. The method is based on the minimization of a penalty function composed by a linear combination of data misfits, model smoothness and magnitude of perturbations. A priori parameters are defined to regularize the solution. The spatial smoothing is controlled by two parameters α and σ, where σ defines the width of a Gaussian smoothing function and α is the weight given to the spatial smoothing term of the misfit function. The magnitude of the model perturbations is controlled by the parameter β and λ, the latter defining the weight of path density.

As we only analyse the results in the areas with good path coverage, the smoothing was mainly controlled by α and σ. After verifying that λ and β did not affect the final solution in the well-resolved parts of the model, they were set to, respectively, 1 and 0.4. The correlation length σ is defined to be of the same size of the cells used for the initial tomographic scheme, that is 25 km.

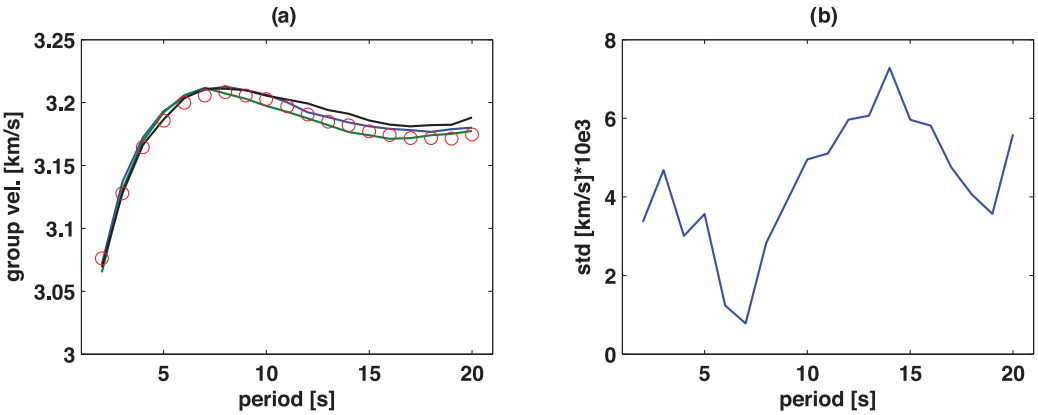

Figure 6. Variability of the average group velocity over different stacking periods. (a) Solid lines: 4-month stacks over January–April (blue), May–August (green), September–December (black). Red circles: 12-month stack. (b) Standard deviation of the velocity 4-months dispersion curve as function of period.

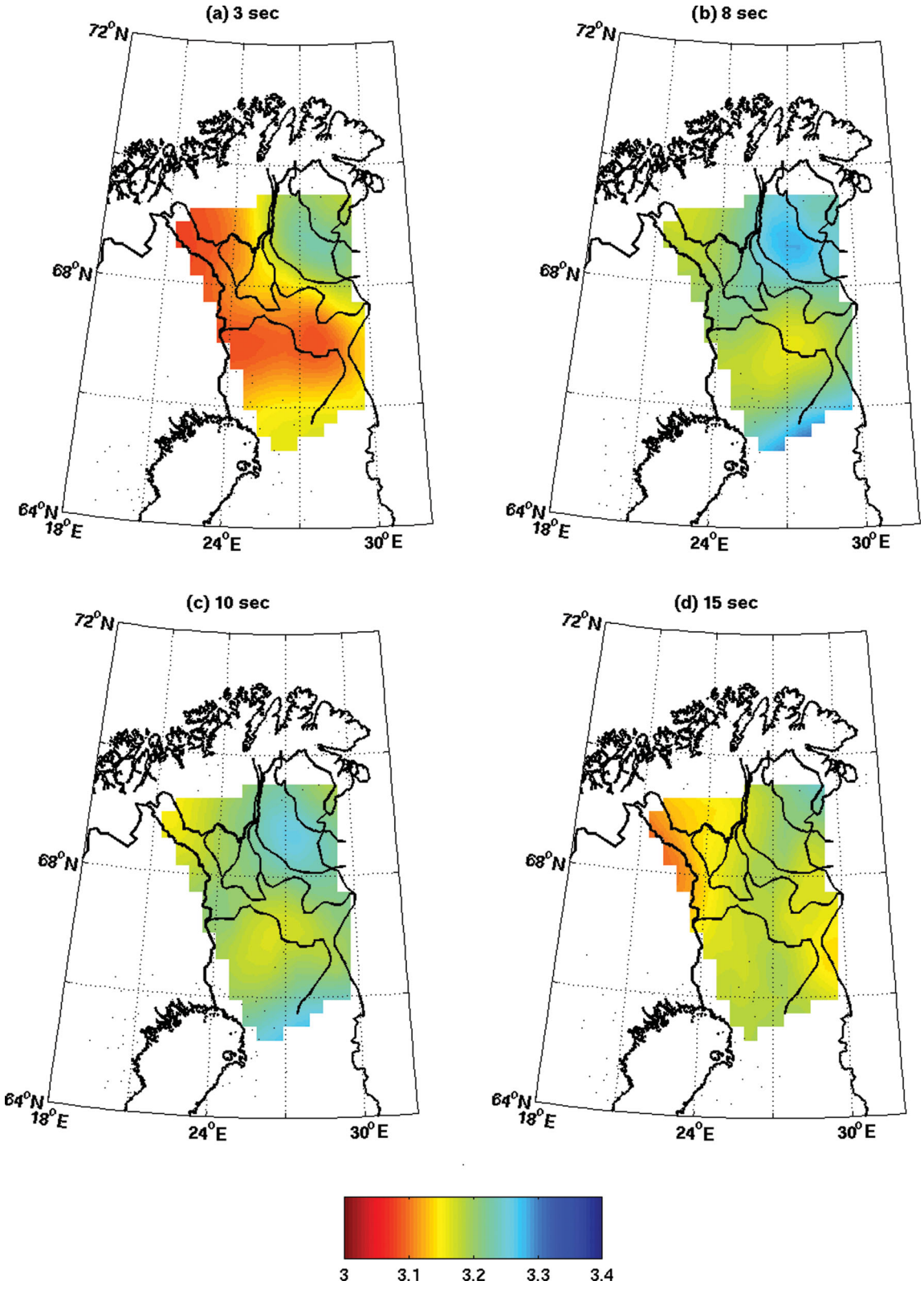

Figure 7. Group velocity map for different periods (indicated over each map). Black lines are the limits of the major geological units of the area. Colourbar is the group velocity in km s^{-1}. For the names of geological units see Fig. 9.

Finally, we chose the value of α based on the variation of the penalty function with α ('L-curve'). Our preferred value of α (200) was chosen to be near the maximum curvature of the L-curve.

Fig. 7 shows the group velocity maps at 3, 8, 10 and 15 s period. At 3 s period, a high velocity anomaly is present in northeastern corner of the model while homogeneous velocities dominate the central part of the map. The limit of the high velocity anomaly

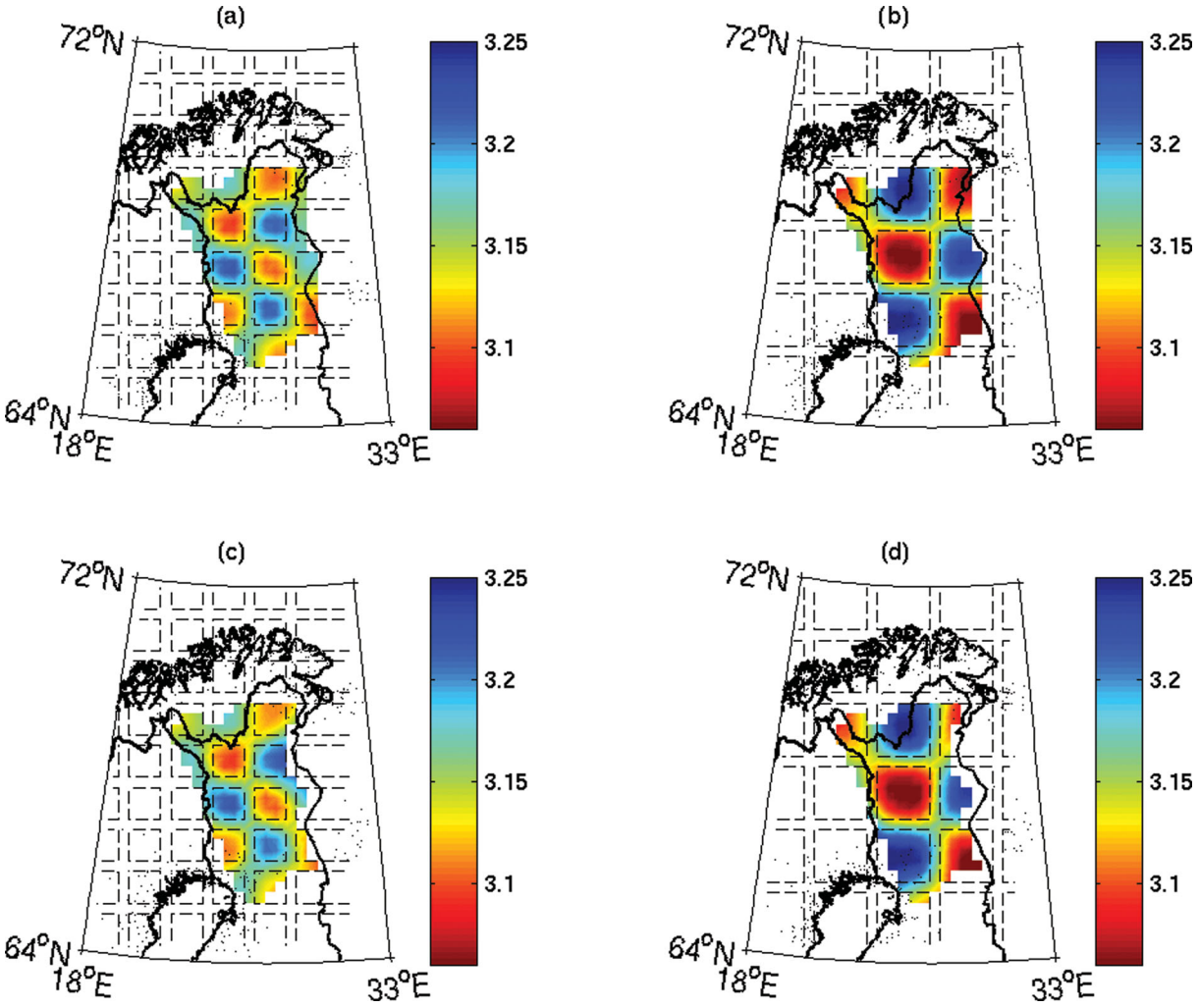

Figure 8. Results of synthetics checkerboard test. The input model is a checkerboard using velocities of 3.04 and 3.25 km s^{-1} (i.e. ±2 per cent) within the squares shown by the dashed lines. (a) 2 s period and 100 km structure size, (b) 2 s period and 150 km structure size, (c) 15 s period and 100 km structure size and (d) 15 s period and 150 km structure size.

coincides with the edge of the Lapland Granulite Terrane ('LGT'). At 5 (Fig. 6b) and 8 (Fig. 6c) s period, the LGT is still present even though the velocity variations are smaller than at 3 s period. At 15 s period, the LGT is still visible, but with a small amplitude and shifted towards the NE.

The resolution depends on both path coverage and model parametrization. We here evaluate the resolution using two independent methods. First, we analyse the resolution matrix to provide the resolution length (in the most poorly resolved direction) at each point of our model following Barmin *et al.* (2001). The resolution is 50–80 km across the central part of the array, and it decreases to 100 km towards the edge where it rapidly decreases to 200 km. We will in the following limit our results to the area where the resolution is better than 100 km. We further carry out checkerboard tests at different periods using two models (structure size of 100 and 150 km) with abrupt velocity variations of ±2 per cent. For each period we use the actual path distribution that is used to obtain the group velocity maps (see selection criteria, Section 3.1). Fig. 8 shows the result of the checkerboard test at 2 and 15 s of period. For structures of 150 km size, the resolution is good for both periods. At 100 km some small smearing is observed especially near the border of the 100 km model at 15 s, but we overall recover the input model in both geometry and amplitude. Overall, our resolution analysis confirms that we can recover structures bigger than 100 km size.

4 3-D *Vs* MODEL

Starting from the group velocity maps, we extracted a dispersion curve at each point of the model. All dispersion curves were then inverted to obtain *S*-wave velocity, using a linearized inversion scheme (Hermann & Ammon 2002). By combining the 1-D *Vs*(*z*) profiles we obtain a 3-D *Vs* model.

4.1 Depth *Vs* inversion

Before the inversion at each grid point, we inverted the average group velocity dispersion curve (Fig. 9b) to define an average crustal *Vs* structure for the region (Fig. 9a). The starting model to invert the average dispersion curve is a slightly modified version of the *Vs* model proposed by Poli *et al.* (2012). The difference resides in the discretization of the upper crust, for which Poli *et al.* (2012) did not have any resolution. We discretized the upper crust (down to 28 km depth) using 17 layers, of varying thickness from 1 to 5 km as function of depth. Between 28 km depth and Moho, at 46 km depth, we use a single layer of 18 km thickness.

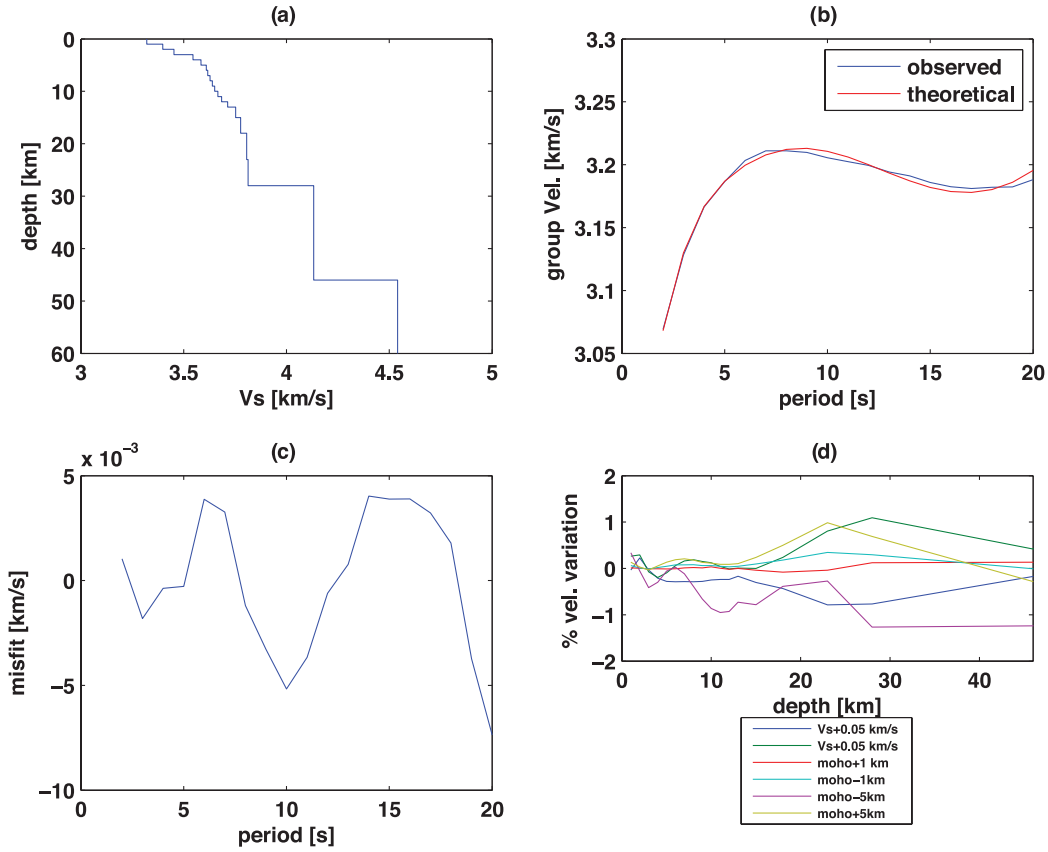

Figure 9. (a) Average shear wave velocity model of the area. (b) Average dispersion curve (blue line) and theoretical curve of the associated with the model of (a). (c) Misfit as a function of period between the two curves of (b). (d) Effect of model parametrization expressed as percent velocity variation respect to the reference model in (a).

The crustal structure has been extensively studied, and both crustal thickness and velocities in the lower crust are well known (see references in Janik *et al.* 2009). We additionally have receiver function estimates from LAPNET (Silvennoinen *et al.* in preparation). Considering the period interval for which we have reliable group velocity maps, we focus the inversion on the upper crust, for which the 3-D structure is less well constrained. With the limited depth resolution of the fundamental mode Rayleigh waves, we impose smooth velocity variations with depth within the top 17 layers. The velocity is allowed to take a large range of values (± 0.2 km s^{-1}) as long as the depth variation is smooth. This will lead, within the given model parametrization, to a very well defined solution. We only allowed for small velocity variations (± 0.02 km s^{-1}) in the thick lowermost crustal layer while mantle velocities were kept constant at a value of 4.54 km s^{-1} (Janik *et al.* 2009). Fig. 9(b) shows the average group velocity curve and the theoretical dispersion curve associated with the output model showed in Fig. 9(a). The overall fit is good (difference less than 0.005 km s^{-1}), as shown in Fig. 9(c).

To verify whether the constraints imposed on crustal thickness and upper mantle velocities significantly influence our upper crustal model, we carried out a series of tests using different Moho depths and upper mantle velocities. Fig. 10(d) shows, as an example, results of such tests on inversion of the average model, which is representative of the tests in individual grid points. We see that erroneous Moho depth and mantle velocity do not product large velocity bias respect to the average model (less than 1 per cent).

Tested the robustness of our inversion strategy, we inverted the *Vs* velocity at each grid point, starting from the average model of Fig. 9(a). As stated before, the Moho depth is fixed at each point, as robust receiver function Moho compilation is present in this area (Silvennoinen *et al.* in preparation). Depth constraints were the same as those imposed for the inversion of the average dispersion curve. The data fit was good for all the grid points. The average data misfit over all grid points and periods is 0.01 km s^{-1} with an rms reduction of 48 per cent.

4.2 *Vs* maps and sections

Our 3-D shear velocity model is presented in Fig. 10 as horizontal slices at different depths and vertical cross-sections. The overall velocity variations are smaller than ± 3 per cent with respect to the average velocity model, with lateral variations mainly present in the upper crust, in agreement with Janik *et al.* (2009). Due to the limited period interval, we will here focus our discussion to the upper 25 km of the crust. The main features of the *Vs* model are the body of high velocities in the NE corner (up to $+2.5$ per cent) and a less pronounced low velocity anomaly (reaching up to -1.5 per cent), most pronounced towards the SE.

The limit of the dominating high *Vs* anomaly coincides at surface with the edge of the Lapland Granulite Terrane (LGT). The lower limit of the high velocity body is almost vertical at the edge, flattens at approximately 10–15 km depth, and finally dips more steeply towards the N–NE. Despite limitations in our resolution, we observe that this geometry is in excellent agreement with results from an active seismic experiment approximately located along profile B–B′ (e.g. Janik *et al.* 2009) which supported a model where the formation

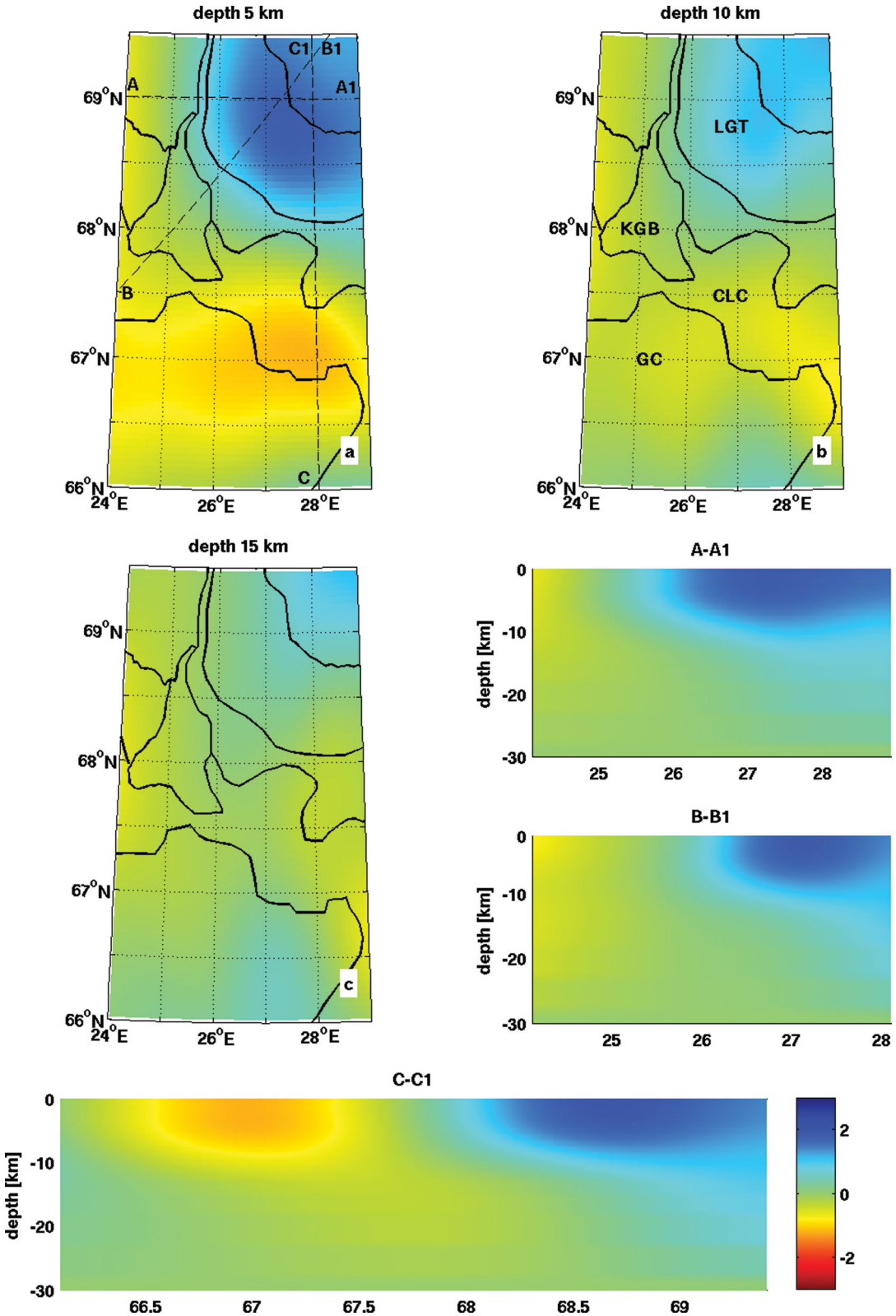

Figure 10. *Vs* velocity maps at 5 (a), 10 (b) and 15 km (c) of depth. Dashed lines in (a) are the geographical location of the sections. The major geological limits are plotted over each maps and the relative name of the geological units is in (b). Colourbar is the velocity variation in per cent respect to the average model. LGT, Lapland Granulite Terrane; KGB, Karasjok-Kittila Greenstones Belt; CLC, Central Lapland Complex; GC, Granitoid complex.

of the Lapland-Kola orogen is associated with a complex series of subduction events, involving three different terranes (Belomorian craton, Karelian craton and Kola craton). We identify these terranes as the low velocity anomaly towards the south (Belomorian craton), the area characterized by slightly higher velocities towards the west (Karelian craton) and the high velocity body associated with the LGT (Kola craton), in the same geographical locations as suggested by Janik *et al.* (2009, fig. 19). The low velocity anomaly associated with the Belomorian craton dips beneath the high velocity body associated with the LGT, compatible with a NS collision event (1.9–2.1 Ga) responsible of the emplacement of the LGT. Our 3-D model confirms that with the exception of LGT, the 3-D structure at depth does not bear direct link to the geological units identified at surface (Karajok-Kittila Greenston Belt, Central Lapland Complex, Granitoid Complex).

5 CONCLUSIONS

ANT here provides constraints on the 3-D geometry of the Archean–Proterozoic contact in northern Finland, as defined at the surface by the edge of the Lapland Granulite belt. Our tomography is in agreement with recent active seismic imaging and tectonic models, which imply a north oriented subduction as proposed by Daly *et al.* (2006) and Janik *et al.* (2009). Different from previous 2-D studies, our model show the power of the 3-D resolution, and permits for the first time to observe some structures that was remained unclear after the 2-D seismic experiments (e.g. the N–S oriented subduction).

Our results demonstrate the value of ANT for seismic imaging also in areas with very small lateral velocity variations, such as cratons. The robustness of the imaging is dependent upon careful correlation processing and analysis of the noise field. It is likely that the processing must be adapted to the study area and the noise sources, so it may not be possible to converge to a uniform approach. In our case, the use of short time windows (Prieto *et al.* 2011; Poli *et al.* 2012; Seats *et al.* 2011; this work) seems particularly adequate to improve the estimate of the Green's function, as it is possible to reject high amplitude signals without strongly decreasing the amount of data. With this approach it is no longer necessary to apply any time normalization such as 1-bit processing or dividing by the moving average of the signal amplitude. An additional advantage is that the output correlations are broadband, so it is relatively easy to retrieve a reliable and continuous group velocity dispersion curve.

Our observed of SNR on azimuth is compatible with previous studies which locate the zones of noise generation principally in the north Atlantic during winter, for both short and long period Rayleigh waves. During the summer months, the main sources are weaker and located towards N–NE, possibly related with retreating ice coverage of the Barents Sea (REF).

While the mechanism of generation of Rayleigh waves is now believed to be relatively well understood, Love wave generation is likely to be more complex, including loading or diffraction effects at seafloor topography. For the second microseismic peak, the source generation of the two types of waves could be collocated, as the maximum SNR is in the same direction. The situation is more complex for the first microseismic peak, where the direction of maximum SNR is different, notably no energy is incoming from the west, that is, related to the north atlantic sources. Surprisingly, the apparent simpler behaviour at high frequency is accompanied by the quasi absence of fundamental mode Love waves, and dominance of a mixture of higher modes. This complexity should lead to caution when high frequency Love waves are used for noise tomography.

ACKNOWLEDGMENTS

We greatly acknowledge support from the QUEST Initial Training network funded within the EU Marie Curie Programme. This study received supported from the ANR BegDy project, the Institut Paul Emil Victor, and European Research Council through the advanced grant 'Whisper' 227507. We thank N. Arndt for useful discussions. The POLENET/LAPNET project is a part of the International Polar Year 2007–2009 and a part of the POLENET consortium, and received financial support from The Academy of Finland (grant No. 122762) and University of Oulu, ILP (International Lithosphere Program) task force VIII, grant No. IAA300120709 of the Grant Agency of the Czech Academy of Sciences, and the Russian Federation: Russian Academy of Sciences (programs No 5 and No 9). The Equipment for the temporary deployment was provided by: RESIF – SISMOB, FOSFORE, EOST-IPG Strasbourg Equipe sismologie (France), Seismic pool (MOBNET) of the Geophysical Institute of the Czech Academy of Sciences (Czech Republic), Sodankyla Geophysical Observatory (FINLAND), Institute of Geosphere Dynamics of RAS (RUSSIA), Institute of Geophysics ETH Zürich (SWITZERLAND), Institute of Geodesy and Geophysics, Vienna University of Technology (AUSTRIA), University of Leeds (UK). POLENET/LAPNET data were prepared and distributed by the RESIF Data Center. The POLENET/LAPNET working group consists of: Elena Kozlovskaya, Teppo Jämsen, Hanna Silvennoinen, Riitta Hurskainen, Helle Pedersen, Catherine Pequegnat, Ulrich Achauer, Jaroslava Plomerova, Eduard Kissling, Irina Sanina, Reynir Bodvarsson, Igor Aleshin, Ekaterina Bourova, Evald Brückl, Tuna Eken Robert Guiguet, Helmut Hausmann, Pekka Heikkinen, Gregory Houseman, Petr Jedlicka, Helge Johnsen, Elena Kremenetskaya, Kari Komminaho, Helena Munzarova, Roland Roberts, Bohuslav Ruzek, Hossein Shomali, Johannes Schweitzer, Artem Shaumyan, Ludek Vecsey, Sergei Volosov. We thank the associate editor and two anonymous reviewers for constructive comments.

REFERENCES

Ardhuin, F., Stutzmann, E., Schimmel, M. & Mangeney, A., 2011. Revealing ocean wave sources of seismic noise, *J. geophys. Res.,* **116,** C0004, doi:10.1029/2011JC006952.

Barmin, M.P., Ritwoller, M.H. & Levshin, A.L., 2001. A Fast and Reliable Method for Surface Wave Tomography, *Pure appl. Geophys.,* **158,** 1351–1375.

Bensen G.D., Ritzwoller M.H., Barmin M.P., Levshin A. L., Lin F., Moschetti M. P, Shapiro N. M. Yang Y., 2007, Processing seismic ambient noise data to obtain reliable broad-band surface wave dispersion measurment, *Geophys. J. Int.*, **169**, 1239–1260.

Campillo, M., 1990. Propagation and Attenuation of Crustal Phase Lg, *Pure appl. Geophys.,* **132,** 1–19, doi:10.1007/BF00874355.

Campillo, M. & Paul, A., 2003. Long-range correlations in the diffuse seismic coda, *Science,* **299,** 547–549.

Daly, J.S., Balagansky, V.V., Timmerman, M.J. & Whitehouse, M.J., 2006. The Lapland-Kola orogen: Paleoproterozoic collision and accretion of the northern Fennoscandian lithosphere, in *European Lithosphere Dynamics,* Vol. 32, pp. 579–598, eds Gee, D.G. & Stephenson, R.A., Geological Society London, Memoirs.

Friederich, A., Kruger, F. & Klinge, K., 1998. Ocean-generated microseismic noise located with the Gräfenberg array, *J. Seism.,* **2,** 47–64.

Froment, B., Campillo, M., Roux, R., Gouédard, P., Verdel, A. & Weaver, R.L., 2010. Estimation of the effect of nonisotropically distributed energy on the apparent arrival time in correlations, *Geophysics,* **75,** SA85–SA93.

Fukao, Y., Nishida, K. & Kobayashi, N., 2010. Seafloor topography, ocean infragravity waves, and background Love and Rayleigh waves, *J. geophys. Res.,* **115,** B04302, doi:10.1029/2009JB006678.

Grob, M., Maggi, A. & Stutzmann, E., 2011. Observations of the seasonality of the Antarctic microseismic signal and its association to sea ice variability, *Geophys. Res. Let.,* **38,** L11302, doi:10.1029/2011GL047525.

Gouédard, P. *et al.*, 2008. Cross-correlation of random fields: mathematical approach and applications, *Geophys. Prospect.,* **56,** 375–393.

Groos, J.C., Bussat, S. & Ritter, J.R.R., 2012. Performance of different processing schemes in seismic noise cross-correlations, *Geophys. J. Int.,* **188,** 498–512.

Herman, R.B. & Ammon, C.J., 2002. *Surface Waves, Receiver Function and Crustal Structure,* St. Louis University.

Hillers, G., Graham, N., Campillo, M., Kedar, S., Landés, M. & Shapiro, N., 2012. Global oceanic microseism sources as seen by seismic arrays and predicted by wave action models, *Geochem. Geophys. Geosyst.,* **13,** Q01021, doi:10.1029/2011GC003875.

Janik, T., Kozlovskaya, E., Heikkinen, P., Yliniemi, J. & Silvennoinen, H., 2009. Evidence for preservation of crustal root beneath the Proterozoic Lapland-Kola orogen (northern Fennoscandian shield) derived from P and S wave velocity models of POLAR and HUKKA wide-angle reflection and refraction profiles and FIRE4 reflection transect, *J. geophys. Res.,* **114,** B06308, doi:10.1029/2008JB005689.

Köhler, A., Weidle, C. & Maupin, V., 2011. Directionality analysis and Rayleigh wave tomography of ambient seismic noise in southern Norway, *Geophys. J. Int.,* **184,** 287–300.

Kozlovskaya, E., Poutanen, M. & Group, P. W., 2006. POLENET/LAPNET-a multi-disciplinary geophysical experiment in northern Fennoscandia during IPY 2007–2008, *Geophys. Res. Abstr.,* **8,** 07049.

Levshin, A., Yanovskaya, T., Lander, A., Buckin, B., Barmin, M., Ratnikova, L. & Its, E., 1989. *Seismic Surface Waves in a Laterally Inhomogeneous Earth,* ed. Keilis-Borok, VI, Kluwer, Norwell, MA.

Pedersen, H., Krüger, F. & the SVEKALAPKO Seismic tomography, 2007. Influence of the seismic noise characteristics on noise correlations in the Baltic shield, *Geophys. J. Int,* **168,** 197–210.

Poli, P., Pedersen, H.A., Campillo, M. & Polenet Lapnet working group, 2012. Emergence of body waves from cross-correlation of seismic noise, *Geophys. J. Int,* **188,** 549–558.

Prieto, G.A., Denolle, M., Lawrence, J.F. & Beroza, G.C., 2011. On the amplitude information carried by ambient seismic field, *Compte Rend. Geosci.,* **3,** 558–570.

Ritzwoller, M.H., Lin, F. & Shen, W., 2011. Ambient noise tomography with a large seismic array, *Compte Rend. Geosci.,* **3,** 558–570.

Sabra, K.G., Gerstoft, P., Roux, P. & Kuperman, W.A., 2005a. Extracting time-domain Green's function estimates from ambient seismic noise, *Geophys. Res. Lett.,* **32,** doi:10.1029/2004GL021862.

Sabra, K.G., Gerstoft, P., Roux, P., Kuperman, W.A. & Fehler, M.C., 2005b. Surface wave tomography from microseisms in southern california, *Geophys. Res. Lett.,* **32,** doi:10.1029/2005GL023155.

Saito, T., 2010. Love-wave excitation due to the interaction between a propagating ocean wave and sea-bottom topography, *Geophys. J. Int.,* **182,** 1515–1523.

Seats, K.S., Lawrence, F.J. & Prieto, A.P., 2011. Improved ambient noise correlations function using Welch's method, *Geophys. J. Int.,* **188,** 513–523.

Shapiro, N.M. & Campillo, M., 2004. Emergence of broadband rayleigh waves from correlations of the ambient seismic noise, *Geophys. Res. Lett.,* **31,** doi:10.1029/2004GL019491.

Shapiro, N.M., Campillo, M., Stehly, L. & Ritzwoller, M.H., 2005. High-Resolution Surface-Wave tomography from ambient seismic noise, *Science,* **307,** 1615–1618.

Silvennoinen, H., Kozlovskaya, E., Kissling, E. & Kosarev, G., 2012. Compilation of Moho boundary for northern fennoscandia, EGU General Assembly 2012, held 22–27 April, 2012 in Vienna, Austria., p. 8566.

Stehly, L., Campillo, M. & Shapiro, N.M., 2006. A study of the seismic noise from its long-range correlation properties, *J. geophys. Res.,* **111,** 1615–1618.

Stehly, L., Fry, B., Campillo, M., Shapiro, N., Guilbert, J., Boschi, L. & Giardini, D., 2009. Tomography of the Alpine region from observations of seismic ambient noise, *Geophys. J. Int.,* **178,** 1338–350.

Stutzmann, E., Schimmel, M., Patau, G. & Maggi, A., 2009. Global climate imprint on seismic noise, *Geochem. Geophys. Geosyst.,* **10,** Q11004, doi:10.1029/2009GC002619.

Verbeke, J., Boschi, L., Stehly, L., Kissling, E. & Michelini, A., 2012. High-resolution Rayleigh-wave velocity maps of central Europe from a dense ambient-noise data set, *Geophys. J. Int.,* **188,** 1173–1187.

Yao, H. & van der Hilst, R., 2009. Analysis of ambient noise energy distribution and phase velocity bias in ambient seismic noise tomography, with application to SE Tibet, *Geophys. J. Int.,* **179,** 1113–1132.

Webb, S., Zhang, X. & Crawford, W., 1991. Infragravity waves in the deep ocean, *J. geophys. Res.,* **96,** 2723–2736.